buildings

MDPI

Article

Effect of Fiber Wrapping Orientations on the Hysteretic Performance of Triple-Tube GFRP–Steel Buckling-Restrained Braces

Jialu Ma [1], Linkai Yang [1], Junkai Lu [2], Wuhan Li [1,3,*] and Jinwei Wang [4]

[1] Institute of Engineering Mechanics, China Earthquake Administration, Harbin 150080, China; jma@iem.ac.cn (J.M.); linkaiyang@iem.ac.cn (L.Y.)
[2] School of Civil Engineering and Transportation, Northeast Forestry University, Harbin 150040, China; lujunkai@nefu.edu.cn
[3] School of Ocean Engineering, Harbin Institute of Technology, Harbin 150090, China
[4] Shenzhen Nanshan Anju Housing Construction and Development Co., Ltd., Shenzhen 518000, China; wangjinwei@nsaj.freeqiye.com
* Correspondence: limingzhong0928@163.com or 25b933032@stu.hit.edu.cn

Abstract

Buckling-restrained braces (BRBs) are widely used to improve the seismic performance of high-rise and long-span structures. This study proposes a triple-tube GFRP–steel buckling-restrained brace (TTGS-BRB) as a lightweight and corrosion-resistant energy-dissipating member for such structures. To investigate its hysteretic behavior, pseudo-static tests were conducted on two scaled TTGS-BRB specimens with different wrapping orientations and end details, and a finite element model was established and validated against the test results for further parametric analyses. The test results showed that the specimen with the $\pm 30^{\circ}$ wrapping configuration and end stiffeners exhibited better hysteretic performance than the 90° specimen without end stiffeners, with the yield force increasing from 147.98 kN to 161.68 kN, the cumulative plastic deformation (CPD) increasing from 7.49 to 209.56, and the cumulative plastic energy (CPE) increasing from 5.25 to 199.12. Based on the validated finite element model, the effects of fiber wrapping orientation, end stiffeners, interfacial gap, P_{cr}/P_y ratio, and steel tube diameter-to-thickness ratio on the hysteretic performance of full-scale TTGS-BRBs were systematically investigated. The numerical results indicate that wrapping orientations within the range of $\pm 0^{\circ}$ to $\pm 45^{\circ}$, end stiffening at both ends, an interfacial gap of 1.5 mm between GFRP and steel, an appropriate P_{cr}/P_y ratio, and a steel tube diameter-to-thickness ratio of less than 24 are beneficial for improving the hysteretic performance of TTGS-BRBs. These findings provide useful references for the design and application of TTGS-BRBs in practical engineering.

Keywords: buckling-restrained brace; GFRP; fiber wrapping orientations; pseudo-static tests; fracture

Check for updates

Academic Editor: Antonio Formisano

Received: 13 March 2026
Revised: 5 April 2026
Accepted: 16 April 2026
Published: 20 April 2026

Copyright: © 2026 by the authors. Licensee MDPI, Basel, Switzerland. This article is an open access article distributed under the terms and conditions of the Creative Commons Attribution (CC BY) license.

1. Introduction

In recent years, with the continuous development of high-rise and long-span structures, seismic resilience has become an increasingly important issue in civil engineering. Buckling-restrained braces (BRBs), as replaceable energy-dissipating members, have attracted extensive attention because they integrate structural support and energy dissipation within a single system and generally exhibit stable hysteretic behavior, cost-effectiveness, and convenient installation. According to Zhou et al. [1], BRBs can be classified into

concrete-filled steel tube (CFST) BRBs, all-steel BRBs, and fiber-reinforced BRBs. Previous studies have demonstrated that BRBs can effectively improve the seismic performance of structures [2–5].

However, conventional BRB systems still suffer from several limitations. In particular, the restraining units in CFST BRBs and all-steel BRBs are often associated with relatively large self-weight and susceptibility to corrosion, which may restrict their application in structures requiring lightweight components and improved durability. To overcome these drawbacks, fiber-reinforced polymer (FRP) materials have gradually been introduced into BRB systems because of their low self-weight and corrosion resistance [6]. Existing studies on FRP-based BRBs have examined BRBs using concrete-infilled GFRP tubes [7], partially CFRP-confined restraining members [8], and assembled restraining systems wrapped with carbon or basalt fiber [9]. In addition, related studies on FRP confinement and FRP tubular strengthening of steel members have shown that FRP-based reinforcement can effectively enhance the stability and buckling resistance of steel braces or compression members [10,11]. These studies confirm the feasibility of FRP-based restraining systems and their potential for improving durability while reducing self-weight.

Nevertheless, current FRP-based BRBs still exhibit several shortcomings. In most reported systems, FRP is combined with concrete, steel tubes, mortar, or other restraining materials rather than being employed as the sole restraining unit [7–11]. As a result, the lightweight and corrosion-resistant advantages of FRP have not yet been fully exploited. Moreover, although Xu [12] proposed an ultra-lightweight BRB restrained by composite materials, square-section configurations may be less suitable for spatial structures, in which circular restraining units generally provide more uniform mechanical properties and simpler joint detailing. Therefore, TTGS-BRBs with circular GFRP restraining units still deserve further investigation.

In the authors' previous study [13], quasi-static tests and finite element analyses were conducted on triple-tube glass fiber-reinforced polymer and steel buckling-restrained braces (TTGS-BRBs), and the results showed that an appropriate P_{cr}/P_y ratio could improve hysteretic performance. However, that study mainly focused on the effect of the P_{cr}/P_y ratio, while the influences of fiber wrapping orientation and other key structural parameters were not systematically clarified. In particular, direct experimental comparisons of different fiber wrapping orientations were lacking, and the effects of end stiffeners(ES), clearance, and diameter-to-thickness ratio on the hysteretic performance of full-scale TTGS-BRBs remained insufficiently understood.

To address these gaps, two scaled TTGS-BRB specimens were designed and fabricated based on the P_{cr}/P_y ratio design method, and pseudo-static tests were conducted to compare the hysteretic behavior of specimens with different fiber wrapping orientations. A finite element model was then established and validated against the test results, and further used to investigate the effects of fiber wrapping orientation, end stiffeners, clearance, P_{cr}/P_y ratio, and diameter-to-thickness ratio on the hysteretic performance of full-scale TTGS-BRBs. Accordingly, this study aims to provide a clearer understanding of the mechanical behavior and design considerations of TTGS-BRBs for practical applications.

2. Experimental Program

2.1. Concept of TTGS-BRB (Harbin Jinruichi Technology Co., Ltd., Harbin, China)

The configuration of the specimen is illustrated in Figure 1. The viewable TTGS-BRB consists of a core steel tube, the inner and outer restraining glass fiber-reinforced polymer (GFRP) tubes, and the flexible pad ring between the steel tube and GFRP tubes.

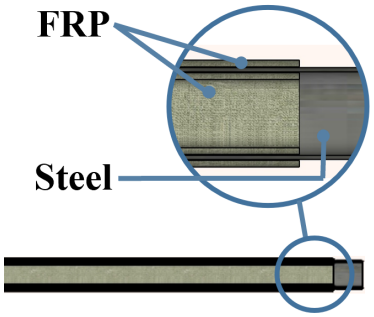


Figure 1. Configuration of TTGS-BRB.

The core is made of Q235 steel tube, and the inner and outer restraining parts are made of wound GFRP tubes. To avoid the axial force on the restraining tube, a suitable clearance was set between the core tube and the restraining tube [14–17], and a flexible pad ring was placed at both ends of the restraining tube to limit the relative position.

2.2. Test Setup and Loading Principle

To investigate the effects of wrapping orientation on the performance of this type of TTGS-BRB, two specimens with different wrapping orientations were tested and compared. The GFRP tubes were formed by using two fiber wrapping methods, namely, Specimen 1 (with single wrapping orientation) and Specimen 2 (with multiple wrapping orientations). For Specimen 1, the wrapping orientation of fibers was perpendicular to the axial direction of the tube ($\theta = 90^\circ$). The wrapping orientation of $\pm 30^\circ$ was adopted for GFRP tubes manufactured by Specimen 2. The clearance between the outer GFRP tube and the steel tube was 1.5 mm, and the same for that between the inner one and the steel tube. Q235-B steel, with an elastic modulus of 182 GPa, was used as the core material for both Specimen 1 and Specimen 2, and its yield strength and ultimate strength were 335 MPa and 397 MPa, respectively. The detailed dimensions of all specimens and the material properties of GFRP are presented in Tables 1 and 2, respectively. As shown in Figure 2, Specimen 1 exhibited overall buckling. Inter-fiber tearing occurred in the middle region of the restraining member, while cracks first appeared at the welds near the ends of the steel core, eventually resulting in tensile fracture. In Table 1, L, D_E, t, D_I, C, and θ represent the length, outer diameter, thickness, inner diameter, gap, and fiber wrapping angle, respectively.

Table 1. Dimensions of specimens.

Specimen	**Specimen 1**			**Specimen 2**		
Component	Core	Outer tube	Inner tube	Core	Outer tube	Inner tube
L (mm)	800	760	760	800	640	640
D_E (mm)	48	63	38	48	63	38
t (mm)	3.5	6	6	3.5	6	6
D_I (mm)	41	51	26	41	51	26
C (mm)		1.5			1.5	
θ		90°			±30°	

Table 2. Material properties of GFRP.

Direction	**Elastic Modulus (MPa)**	**Shear Modulus (MPa)**	**Tension Strength (MPa)**	**Shear Strength (MPa)**
Axial	40.4	3160	74.3	44.7
Normal	5100	3160	20.3	43.0



Figure 2. Failure modes of the specimens.

As shown in Figure 3, a series of pseudo-static tests were conducted on the specimen with a 250 ton MTS electro-hydraulic servo testing machine to investigate the hysteretic behavior, compression strength adjustment factor, energy dissipation capacity and failure modes. Two linearly variable displacement transducers (LVDTs) installed at the loading end of specimens were used to record the axial deformation of the steel tube. The restoring forces were obtained automatically by the MTS system. The specimens were loaded on an increased level gradually, and the corresponding amplitude was as follows: $L/600$, $L/300$, $L/200$, $L/150$, $L/100$, $L/75$, and $L/50$. Each displacement amplitude was performed twice, as shown in Figure 4.

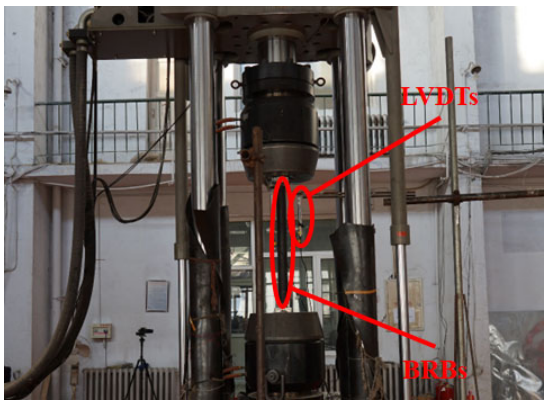


Figure 3. Test setup.

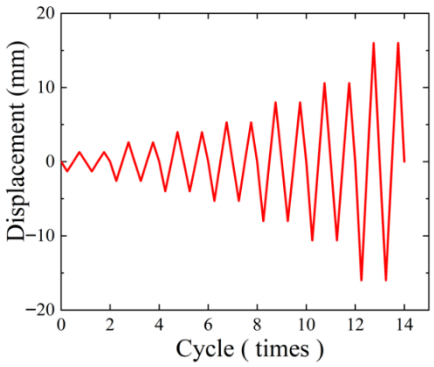


Figure 4. Loading principle.

3. Hysteretic Behavior and Energy Dissipation Analysis

3.1. Hysteretic Performance

The hysteretic curves of two specimens are presented in Figure 5. The compressed states of the specimens are displayed in the negative direction. The failure process of Specimen 1 and Specimen 2 can be divided into three typical stages.

In the first stage, Specimen 1 displayed stable hysteretic behavior during the first two loading levels ($L/600$, $L/300$). In the second stage, the slight cracking and flexural buckling of the outer GFRP tube were observed for the specimens under compression in the fifth cycle ($L/200$). In the third stage, the lateral bending of the specimens became more

serious with the further increase in axial deformation. The test was ceased till the fracture of the weld between the steel tube and the lower end plate was induced at subsequent loading ($L/75$) from the compression to tension excursion.

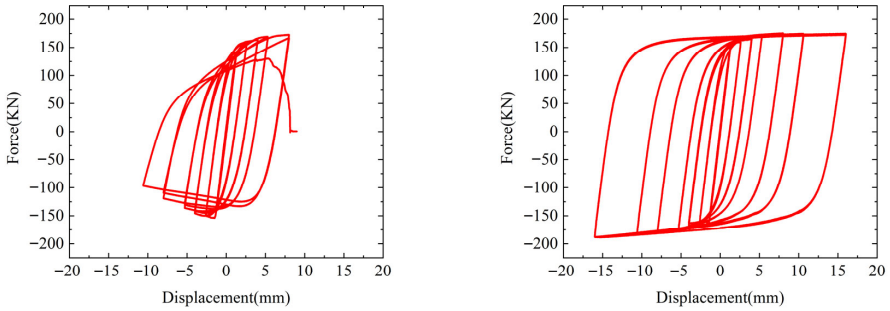


Figure 5. Hysteretic curve of specimens: (**a**) Specimen 1; (**b**) Specimen 2.

However, Specimen 2 in the above tests showed stable and good hysteretic energy dissipation performance in the whole loading cycle, and the hysteretic curves were full and symmetrical, and the stiffness did not degenerate. In the first stage, Specimen 2 displayed stable hysteretic behavior during the first five loading levels ($L/600$, $L/300$, $L/200$, $L/150$, $L/100$). In the second stage, the constraining tube debonded in the tensile cycle at an $L/75$ displacement ratio. In the third stage, during the second compressive cycle at a $L/50$ displacement ratio, local buckling emerged in the unrestrained transition zone near the ends. It is worth noting that Specimen 2 did not exhibit global buckling throughout the test, and the surfaces of the constraining tube remained crack-free.

As shown in Figure 5a, Specimen 1 exhibited stable hysteretic energy dissipation behavior without noticeable stiffness degradation prior to the $L/200$ loading cycle. However, a marked stiffness reduction occurred during the first compressive loading of the $L/200$ cycle. With further loading, the specimen stiffness progressively degraded, the pinching of the compressive-side hysteretic response became more pronounced, and the tension–compression asymmetry became evident. Ultimately, Specimen 1 experienced complete failure as a result of end fracture during the first tensile loading of the $L/75$ cycle.

The results show that Specimen 2 (with multiple wrapping orientations) has obvious performance advantages over Specimen 1 (with a single wrapping orientation).

As seen in Figure 6, the degeneration of the stiffness and strength of both specimens was observed under compression after the first four cycles were completed.

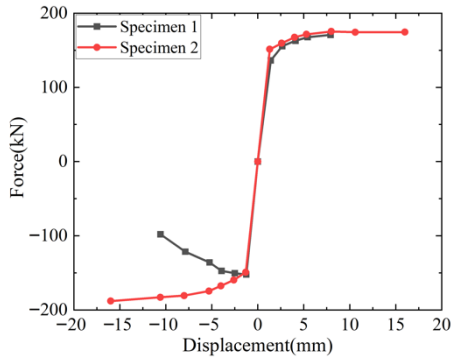


Figure 6. Comparison of skeleton curves.

The constraining tube of Specimen 1 cracks before the constraining tube of Specimen 2, resulting in global buckling failure and fracture at the end. The hysteretic curve

of Specimen 2 is full and does not have global buckling instability, but local buckling occurs first.

The wrapping method adopted by Specimen 1 is 90° wrapping, while Specimen 2 adopts a bidirectional 30° wrapping. Therefore, although the core steel tube is the same as Specimen 2, the test phenomenon shows that Specimen 1 has the global buckling first, followed by the yield fracture of the core steel, and the yield strength of the core steel cannot be fully utilized by means of the design of the constraining tube. While supporting Specimen 2, the core steel has yielded, and the whole has not produced obvious buckling instability, which means that the yield strength of the core steel has been fully utilized.

Specimen 1 did not include end stiffeners, while Specimen 2 was provided with end stiffeners. Owing to the abrupt change in stiffness, significant stress concentration occurred at the welded region of Specimen 1, which eventually led to pull-off failure during the test. By contrast, the incorporation of end stiffeners in Specimen 2 effectively alleviated this issue.

The difference in hysteretic performance between Specimen 1 and Specimen 2 could also be explained by the P_{cr}/P_y ratio design methodology. The P_{cr}/P_y ratio design method is proposed by Wantanabe [18], and the P_{cr}/P_y ratio is the ratio of the critical buckling capacity of the BRBs to the yield bearing capacity of the core steel. In the confinement ratio design methodology, the distinction between bidirectional and unidirectional fiber wrapping orientations is attributed to differences in the elastic modulus of the confinement sleeve, while the presence or absence of end stiffeners is correlated with variations in the calculated core length. Consequently, both bidirectional fiber wrapping orientations and end stiffeners lead to an increase in the confinement ratio within this design framework.

The $P_{\mathrm{cr}}/P_{\mathrm{y}}$ ratio of Specimen 1 is 0.28. The calculation results of the formula show that the yield of the core steel member of the specimen occurs before the global buckling instability caused by the failure of the GFRP tube. The test results also prove that the global buckling of Specimen 1 occurs first, and then the core end causes the yield fracture.

The $P_{\mathrm{cr}}/P_{\mathrm{y}}$ ratio of Specimen 2 is 1.74. The formula calculation results show that the global buckling caused by the failure of the GFRP tube of the specimen occurs earlier than that of the core steel, and the test results also prove that the constrained member of the Specimen 2 fails to unglue first, and then the core steel has local buckling.

This is consistent with the conclusion that the $P_{\mathrm{cr}}/P_{\mathrm{y}}$ ratio should be more than 1.5, as suggested in the previous work [16], because Specimen 1 is less than the recommended value, and Specimen 2 is more than the recommended value, so the hysteretic ability of Specimen 1 is far less than that of Specimen 2.

3.2. Energy Dissipation

The main seismic performance indices, including yield force P_{y}, yield displacement of the support δ_{y}, ultimate load-carrying capacity P_{u}, compressive limit bearing capacity P_{uc}, compression strength adjustment factor β, ductility coefficient μ, cumulative plastic deformation (CPD) and cumulative plastic energy (CPE), are summarized in Table 3. The specific calculation formulas of parameters can be referred to papers [19,20].

The ductility coefficient reflects the plastic deformation capacity of the BRBs and is an important basis for evaluating the seismic performance of the BRBs. The ductility coefficient of TTGS-BRB shall not be less than 10 as stipulated in the Code for Seismic Design of Building Steel Structures in the United States [21]. The ductility coefficient μ of Specimen 1 is about 1.8, which is far from the standard requirement. The ductility coefficient of Specimen 2 is about six times that of Specimen 1 and more than 10, indicating that the specimens have sufficient plastic deformation capacity.

CPE coefficient reflects the ratio of the total hysteretic energy dissipation accumulated by the BRBs during the low-cycle reciprocating loading to the elastic strain energy and represents the cumulative seismic energy dissipation capacity of the support.

Table 3. Main seismic performance indices.

Test Specimen	P_y (kN)	δ_y (mm)	P_u (kN)	P_{uc} (kN)	P_{ut} (kN)	μ	β	CPD	CPE
Specimen 1	147.98	1.43	194.15	153.94	158.95	1.818	0.97	7.49	5.25
Specimen 2	161.68	1.44	194.15	188	175.36	11.11	1.07	209.56	199.12

According to ANSI/AISC 341 [21], the cumulative plastic deformation (CPD) of a BRB should not be less than 200. As shown in Table 3, the CPD of Specimen 1 was far below this limit because of premature failure after global buckling, indicating that it did not meet the CPD requirement. In contrast, the CPD of Specimen 2 exceeded 200, indicating that it met the CPD requirement. Moreover, the CPD and CPE values of Specimen 2 were much higher than those of Specimen 1, suggesting superior cumulative deformation and energy dissipation capacity. Here, CPE is discussed only as a comparative indicator, since no explicit requirement for CPE is given in reference [21].

4. Finite Element Model and Verification

To provide a better understanding of the hysteretic behavior and stability of specimens, a parametric study using the software ABAQUS 2018 is conducted. The explicit analysis step was used to simulate the hysteretic mechanical properties of the TTGS-BRB in pseudo-static tests [22–27]. Some specimens with end stiffeners were considered in this numerical study. The total length of the steel tube was assumed to be 4300 mm, and its outside diameter and thickness were 121 mm and 4 mm, respectively. Both steel tube and GFRP tubes were modeled using four-node shell elements with the reduced-integration technique (S4R), with 30 units in the radial direction. The elastic lamina model and 'Hashin Damage' criterion were employed to simulate the multiple-layer GFRP material due to the anisotropy for the composite layer materials [13], and the corresponding parameters can be obtained by the material properties of GFRP listed in Table 2. The kinematic strain hardening property was considered for the steel tube in the nonelastic material property to account for an accurate cyclic hardening behavior, and the post-yield modulus was defined as 2% of Young's modulus. A cyclic, axial load was applied to both ends of the steel tube in the analysis using the same displacement principle presented in Figure 4. The surface-to-surface contact interaction was defined between the steel tube and the GFRP tube. The normal contact behavior at the interface was modeled using the "Hard Contact" formulation, while the tangential behavior was described by a Coulomb friction model with a penalty friction coefficient of 0.3. The selected friction coefficient was adopted with reference to ref. [28], in which similar contact assumptions were used for the numerical simulation of GFRP–steel or composite-material buckling-restrained braces. This contact formulation permits the separation between the steel tube and the GFRP tubes. The occurrence of interface separation is explicitly indicated when the contact pressure diminishes to zero. Such contact characterization facilitates the development of higher-order buckling modes in the steel tube. The FE (Finite Element) model is shown in Figure 7.

A structured meshing technique was employed in the finite element model. The mesh discretization was selected with reference to [28] and further determined through preliminary trial calculations. Finally, approximately 30 elements were arranged along the circumference of the tube. Both the steel core and the restraining unit were modeled using the four-node reduced-integration shell element S4R, which is suitable for both thin-

and thick-shell structures, incorporates hourglass control, and allows for finite membrane strains. According to ref. [28] and the present trial calculations, the adopted mesh scheme was considered adequate for achieving a reasonable balance between computational accuracy and efficiency.

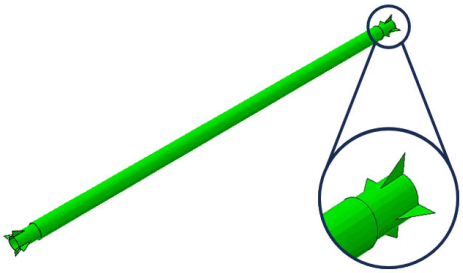


Figure 7. FE model of TTGS-BRB.

Figure 8a presents a comparison between the experimental and simulated failure modes of Specimen 1. The simulated failure mode agrees well with the experimental result. Specifically, Specimen 1 exhibits single-wave buckling at the mid-length.

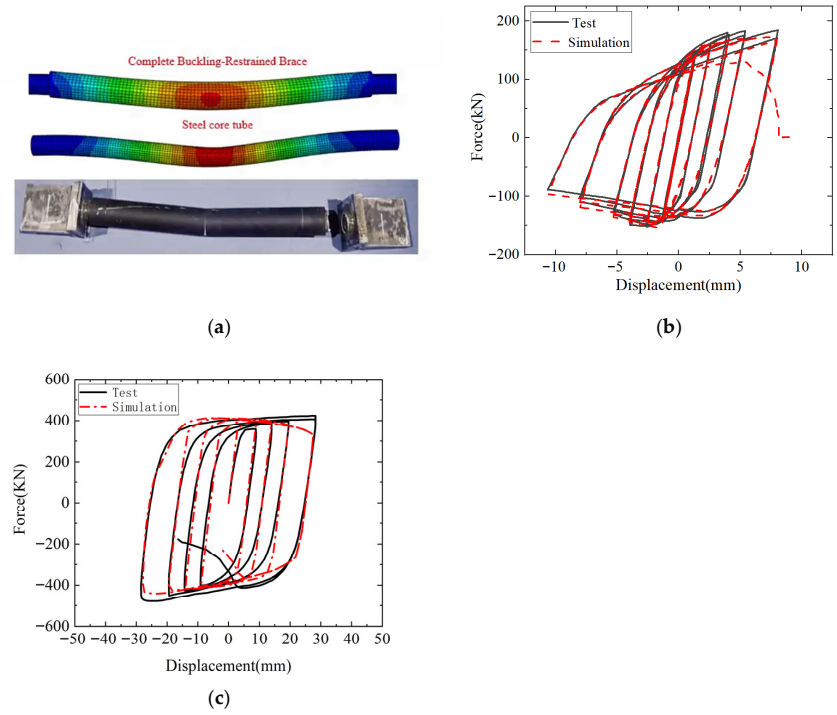


Figure 8. Verification of the FE model: (**a**) Comparison between the failure mode of Specimen 1 in the test and the simulation; (**b**) comparison of hysteresis curves of Specimen 1; (**c**) comparison of hysteresis curves of the specimen reported in ref. [12].

Figure 8b,c compare the experimental and numerical hysteretic curves of Specimen 1 and the specimen reported in ref. [12], respectively. As shown in Figure 8b, the simulated hysteretic response of Specimen 1 agrees well with the test result under the same loading protocol. To quantitatively evaluate the agreement between the experimental and FE hysteretic responses, the main displacement reversal points of the hysteresis curves were extracted for one-to-one comparison. For Specimen 1, the force-response mean absolute error (MAE), root mean square error (RMSE), and mean absolute percentage error (MAPE) were 6.75 kN, 8.02 kN, and 9.18%, respectively, while the corresponding displacement MAE, RMSE, and MAPE were 0.034 mm, 0.053 mm, and 0.679%, respectively. The corre-

lation coefficients reached 0.9991 for force and 0.99997 for displacement. In addition, the overall peak tensile force predicted by the FE model was 184.33 kN, compared with the experimental value of 172.81 kN, corresponding to a relative error of 6.67%, whereas the overall peak compressive force was 152.84 kN in the FE simulation and 153.94 kN in the test, corresponding to a relative error of 0.72%. For the specimen reported in ref. [12], as shown in Figure 8c, the force-response MAE, RMSE, and MAPE were 28.24 kN, 34.89 kN, and 8.76%, respectively, while the corresponding displacement MAE, RMSE, and MAPE were 0.180 mm, 0.302 mm, and 1.17%, respectively. The correlation coefficients were 0.9963 for force and 0.9999 for displacement. Moreover, the overall peak tensile force predicted by the FE model was 413.27 kN, compared with the experimental value of 406.86 kN, corresponding to a relative error of 1.58%, whereas the overall peak compressive force was 441.27 kN in the FE simulation and 451.51 kN in the test, corresponding to a relative error of 2.27%. These results indicate that the FE model can reasonably reproduce the main hysteretic characteristics of both Specimen 1 and the specimen reported in ref. [12].

5. Case Studies of Triple-Tube TTGS-BRB

After establishing a reliable finite element model through model verification, this paper carries out the parameter research of BRB, including fiber wrapping orientations, end stiffeners, clearance, P_{cr}/P_y ratio of the steel tube and diameter–thickness ratio. The fiber wrapping orientations refer to the fiber wrapping orientations of the GFRP tube, and the appropriate fiber wrapping orientations can give full play to the strength of the fiber. End stiffeners refer to the steel ribs at both ends of the core, which can avoid abrupt changes in stiffness at both ends of the core material. The clearance refers to the clearance between the GFRP tube and the steel tube, and enough clearance can avoid the global instability of the steel tube. The P_{cr}/P_y ratio is the ratio of the critical buckling capacity of the BRBs to the yield bearing capacity of the core steel, and the appropriate P_{cr}/P_y ratio can make full use of its strength. The diameter–thickness ratio is used to describe the relationship between the outer diameter and thickness of the steel tube, which directly affects the moment of inertia of the section and the local stability of the steel tube. The results presented in this section correspond to numerical analyses based on the finite element (FE) model.

5.1. Fiber Wrapping Orientations

Figure 9 shows the skeleton curves of braces with different fiber wrapping orientations. The results indicate that the buckling load and overall stability generally improve as the wrapping orientation decreases. For the single wrapping configuration, stable responses were mainly obtained when the wrapping orientation was within 0–30°. At a displacement of −86 mm, the compressive skeleton loads of the 0°, 10°, 25°, and 30° cases ranged from −440.80 to −443.98 kN, whereas the 35° case decreased to −366.73 kN. When the wrapping orientation increased to 45° and above, the stability deteriorated significantly. In contrast, for the multiple wrapping configuration, stable responses were maintained over a wider range. At −86 mm, the compressive skeleton loads of the ±10° to ±45° cases remained between −440.55 and −441.88 kN, while the ±50° and ±60° cases showed a significant reduction at larger deformation levels. A direct comparison further shows that multiple wrapping provides more effective restraint than single wrapping. For example, at a comparable angle of about 45°, the compressive load of the ±45° case reached −410.65 kN at −57.33 mm, whereas that of the single 45° case was only −161.48 kN. These results indicate that multiple wrapping orientations are more favorable for improving the flexural capacity and restraining performance of the GFRP tube.

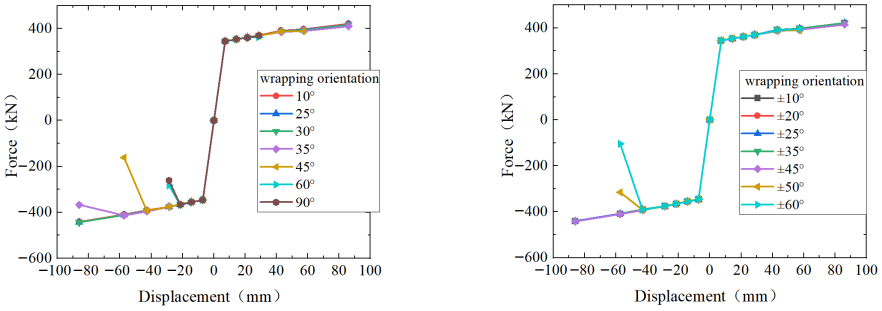


Figure 9. Effect of fibre wrapping orientation: (**a**) Specimen with single wrapping fibre orientation; (**b**) specimen with multiple wrapping fibre orientation.

5.2. End Stiffeners

Figure 10a shows the hysteretic properties of specimens with and without end stiffeners (ES) with different clearances respectively. The hysteretic properties of the components with end stiffeners are better than those without end stiffeners. Under axial tension pressure with little difference, the braces with end stiffeners have larger deformation and better ductility. This is because the end stiffeners increase the stiffness of the supporting end, so that the deformation of the core steel can be more fully developed in the middle. In the end, the GFRP tube can play a more effective role, and without the support of the end stiffeners, the GFRP tube fails to play a restraint role at both ends due to the uniform stiffness of the middle and both ends of the core steel.

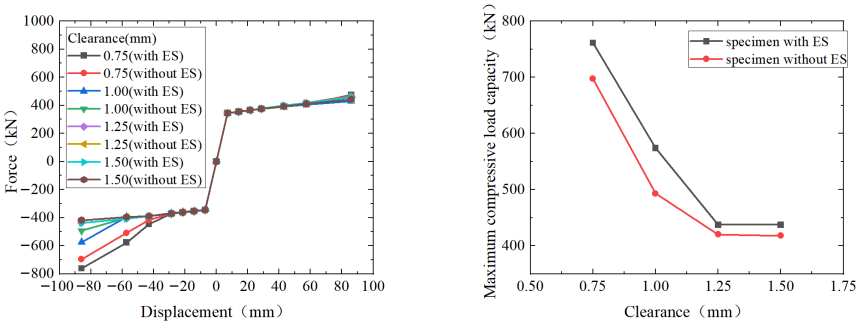


Figure 10. Hysteretic property of different specimens: (**a**) Skeleton curves; (**b**) comparison between specimens with and without end stiffeners.

This situation is particularly obvious when the distance between the GFRP and steel tube is less than 1.00 mm, and it can be seen that the smaller the distance, the greater the abrupt changes in stiffness between the steel tube without GFRP at the end and the steel tube with GFRP in the middle, so the greater the difference in hysteretic properties. When the clearance between the GFRP and the steel tube reaches 1.25 mm or more, the problem of abrupt changes in stiffness is well solved.

Figure 10b shows the change in the maximum compressive load capacity of the specimen with or without stiffeners as the clearance increases. It can be seen that the maximum compressive load capacity of the specimen is greatly influenced by the end stiffener when the clearance is less than 1.00 mm, while the effect is less when the clearance is greater than 1.25 mm.

5.3. Clearance

As shown in Figure 11, the braces exhibited stable hysteretic behavior without obvious strength or stiffness degradation during cyclic loading. For clearances of 1.5–5.0 mm, the hysteretic loops and skeleton responses were generally close to each other. For example, at a compressive displacement of −57.33 mm, the compressive loads for clearances from 1.5 to 5.0 mm ranged only from −409.90 to −414.14 kN, with a maximum difference of about 1.0%. At a compressive displacement of −86 mm, the corresponding loads ranged from −441.90 to −451.21 kN, and the maximum difference was about 2.1%. Similarly, at a tensile displacement of 57.33 mm, the tensile loads for clearances from 1.5 to 5.0 mm ranged from 394.32 to 404.08 kN, corresponding to a difference of about 2.4%. These results indicate that, within this range, the influence of clearance on the global hysteretic response is limited.

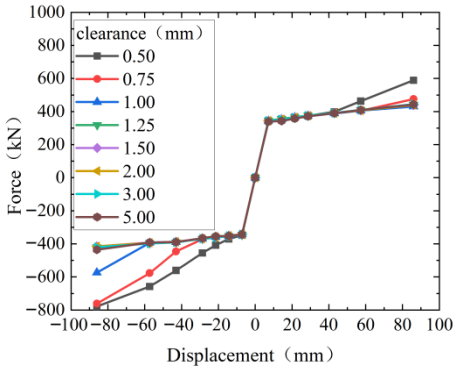


Figure 11. Skeleton curves with different clearance.

In contrast, when the clearance was reduced to 1.0 mm and especially 0.5 mm, the load response increased significantly. At −86 mm, the compressive load of the 0.5 mm case reached −589.38 kN, which was about 33.4% higher than that of the 1.5 mm case (−441.90 kN). At 86 mm, the tensile load of the 1.0 mm case reached 598.91 kN, which was about 43.2% higher than that of the 1.5 mm case (418.17 kN). This indicates that excessively small clearance does not provide sufficient transverse space for the middle steel tube, resulting in intense contact between the steel tube and the GFRP tube and causing the two components to resist axial load together. Although a smaller clearance can provide a stronger restraining effect, it also imposes higher manufacturing requirements. Therefore, considering both restraining efficiency and fabrication feasibility, a clearance of about 1.5–2.5 mm is suggested for the proposed brace.

5.4. P_{cr}/P_y Ratio

Figure 12 shows that the effect of slenderness ratio depends strongly on the P_{cr}/P_y ratio. When P_{cr}/P_y =1.40, the GFRP tube provides sufficient restraint, and the brace with a smaller slenderness ratio exhibits a much higher load-carrying capacity. For example, the tensile and compressive skeleton loads increased from 166.24 to 779.23 kN at 86 mm and from −176.32 to −833.80 kN at −86 mm, respectively, as the slenderness ratio decreased from 130.75 to 69.47. In contrast, when P_{cr}/P_y =1.05, a smaller slenderness ratio still produced higher stiffness before instability, but the corresponding braces lost stability at smaller displacement amplitudes. For instance, the cases with slenderness ratios of 78.93 and 69.47 could not maintain a stable response beyond ±28.67 mm. This indicates that a smaller slenderness ratio is beneficial only when the P_{cr}/P_y ratio is sufficiently large; otherwise, insufficient restraint stiffness makes the brace more susceptible to premature global buckling.

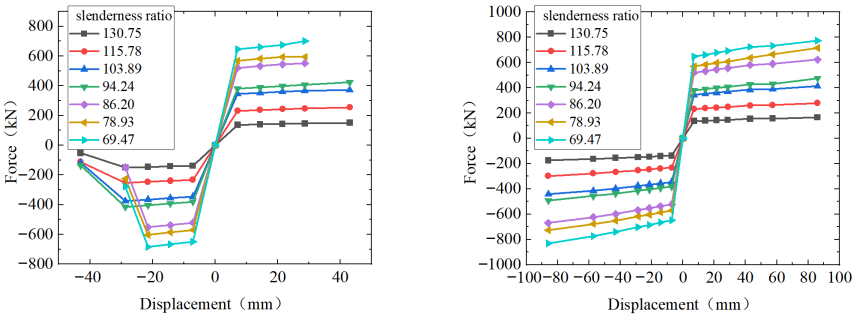


Figure 12. Influence of P_{cr}/P_y: (**a**) P_{cr}/P_y = 1.05; (**b**) P_{cr}/P_y = 1.40.

5.5. Diameter–Thickness Ratio of the Steel Tube

Figure 13 shows that the skeleton curves with different diameter-to-thickness ratios remain generally stable without obvious strength degradation, while the load-carrying capacity increases markedly as the diameter-to-thickness ratio decreases. With the outer diameter of the core steel tube kept constant at 121 mm, a smaller diameter-to-thickness ratio corresponds to a larger wall thickness and cross-sectional area. For example, when the diameter-to-thickness ratio decreases from 60.5 to 12.1, the tensile skeleton load at 86 mm increases from 213.49 kN to 984.33 kN, and the compressive skeleton load at −86 mm increases from −225.86 kN to −1040.88 kN. These results indicate that a smaller diameter-to-thickness ratio is beneficial for improving the load-carrying capacity of TTGS-BRBs. However, an excessively large diameter-to-thickness ratio means a thinner tube wall, which may increase the risk of local instability at the unconstrained end under large deformation. Therefore, the diameter-to-thickness ratio is suggested to be less than 24.

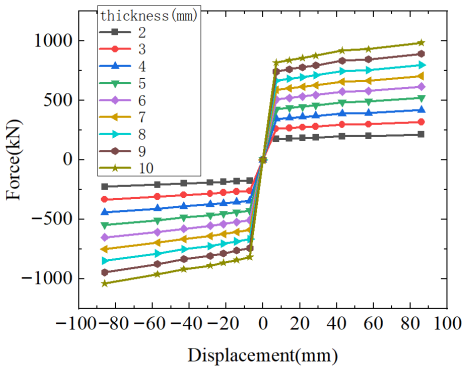


Figure 13. Skeleton curve of the diameter–thickness ratio of the steel tube.

6. Conclusions

This study investigated the hysteretic behavior of TTGS-BRBs through tests on two specimens with different fiber wrapping orientations and a finite element parametric study considering five key design parameters. Within the scope of the present experimental and numerical investigation, the following conclusions can be drawn:

1. Compared with the specimen using a single fiber wrapping orientation, the TTGS-BRB specimen with multiple fiber wrapping orientations exhibited more stable hysteretic behavior and improved deformation capacity. The test results suggest that the use of multiple wrapping orientations is beneficial for delaying local damage development and reducing the likelihood of premature fracture under cyclic loading.
2. The results indicate that the fiber wrapping orientation has a non-negligible influence on the global restraining effect of the composite tube and therefore should be considered in design, particularly when evaluating the equivalent elastic modulus and the

corresponding P_{cr}/P_y ratio. In addition, the stiffness contribution of the end stiffener should be accounted for when determining the effective computational length of the steel tube.

3. The ABAQUS 2018 finite element model reproduced the main failure characteristics and the overall hysteretic response observed in the tests with reasonable agreement. This suggests that the proposed model can be used as a useful tool for preliminary parametric evaluation of TTGS-BRB behavior within the investigated parameter range. However, its predictive capability should still be interpreted with caution because the experimental validation was based on only two specimens.
4. The parametric study shows that, within the investigated ranges, TTGS-BRBs tend to achieve better hysteretic performance when multiple fiber wrapping orientations between $\pm 0^\circ$ and $\pm 45^\circ$ are adopted, end stiffening is provided at both ends, the interfacial gap between the GFRP and steel layers is controlled around 1.5 mm, the slenderness ratio is selected according to the target P_{cr}/P_y requirement, and the diameter-to-thickness ratio is kept below 24. These observations should be regarded as preliminary design implications rather than universally applicable recommendations.
5. It should be noted that the conclusions of this study are subject to several limitations, including the small number of test specimens, possible uncertainties in material properties, manufacturing and assembly imperfections, and the simplifications adopted in the finite element modeling. Therefore, further experimental studies with a broader specimen matrix are required before the above findings can be generalized for design applications.

Author Contributions: Conceptualization, J.M. and J.L.; methodology, J.M., L.Y. and J.L.; validation, J.W.; investigation, J.M. and J.L.; resources, L.Y.; data curation, W.L. and J.W.; writing—original draft, J.M., L.Y. and W.L.; writing—review and editing, J.M., L.Y., J.L. and W.L.; visualization, J.M.; project administration, J.M. and J.W. All authors have read and agreed to the published version of the manuscript.

Funding: The research presented in this paper was jointly supported by the Scientific Research Fund of Institute of Engineering Mechanics, China Earthquake Administration (Grant No. 2020D04 & 2023C08) and the Natural Science Foundation of Heilongjiang Province, China (Grant No. LH2023E018).

Data Availability Statement: The original contributions presented in this study are included in the article. Further inquiries can be directed to the corresponding author. The data that support the findings of this study are available on request from the corresponding author, upon reasonable request.

Acknowledgments: The authors would like to thank the reviewers for their comments on this article.

Conflicts of Interest: Author Jinwei Wang was employed by Shenzhen Nanshan Anju Housing Construction and Development Co., Ltd. The remaining authors declare that the research was conducted in the absence of any commercial or financial relationships that could be construed as a potential conflict of interest.

References

1. Zhou, Y.; Shao, H.; Cao, Y.; Lui, E.M. Application of buckling-restrained braces to earthquake-resistant design of buildings: A review. *Eng. Struct.* **2021**, *246*, 112991. [CrossRef]
2. Kant, R.; Al Agha, W.; Thakur, M.S.; Umamaheswari, N. Comparative study on seismic performance of steel-concrete composite structure without and with buckling-restrained braces. *Mater. Today Proc.* **2022**, *56*, 2134–2144. [CrossRef]
3. Wang, B.; Jiang, W.; Wang, J.; Li, B.; Zhao, C.; Liu, W. Studies on cyclic tests of assembly CFST composite frames with BRB. *Earthq. Eng. Struct. Dyn.* **2024**, *54*, 976–992. [CrossRef]

4. Jiang, T.; Dai, J.; Yang, Y.; Liu, Y.; Bai, W. Study of a new-type of steel buckling-restrained brace. *Earthq. Eng. Eng. Vib.* **2020**, *19*, 239–256. [CrossRef]
5. Ren, F.; Zhou, Y.; Zhang, J.; Lin, S. Experimental study on seismic performance of CFST frame structures with energy dissipation devices. *J. Constr. Steel Res.* **2013**, *90*, 120–132. [CrossRef]
6. Less, T.; Demir, A.; Sezen, H. Structural performance and corrosion resistance of fiber reinforced polymer wrapped steel reinforcing bars. *Constr. Build. Mater.* **2023**, *366*, 130176. [CrossRef]
7. Sun, H.; Jia, M.; Zhang, S.; Wang, Y. Study of buckling-restrained braces with concrete infilled GFRP tubes. *Thin Walled Struct.* **2019**, *136*, 16–33. [CrossRef]
8. Bashiri, M.; Toufigh, V. Numerical and experimental investigation on a BRB confined with partially carbon fiber reinforced polymer (CFRP). *Eng. Struct.* **2020**, *223*, 111150. [CrossRef]
9. Jia, M.; Yu, X.; Lu, D.; Lu, B. Experimental research of assembled buckling-restrained braces wrapped with carbon or basalt fiber. *J. Constr. Steel Res.* **2017**, *131*, 144–161. [CrossRef]
10. Gao, X.Y.; Balendra, T.; Koh, C.G. Buckling strength of slender circular tubular steel braces strengthened by CFRP. *Eng. Struct.* **2013**, *46*, 547–556. [CrossRef]
11. Harries, K.A.; Peck, A.J.; Abraham, E.J. Enhancing stability of structural steel sections using FRP. *Thin Walled Struct.* **2009**, *47*, 1092–1101. [CrossRef]
12. Xu, X. Research and Experimental Study on Mechanical Behaviors of an Ultra-Lightweight BRB Restrained by Composite Material. Master's Thesis, Tsinghua University, Beijing, China, 2015. (In Chinese)
13. Ma, J.; Wang, J.; Zhang, L.; Zhi, X. Pseudo-static tests and numerical investigations of triple-tube glass fiber-reinforced polymer and steel buckling-restrained braces. *Adv. Mech. Eng.* **2020**, *12*, 168781402092205. [CrossRef]
14. Chou, C.-C.; Chen, S.-Y. Subassemblage tests and finite element analyses of sandwiched buckling-restrained braces. *Eng. Struct.* **2010**, *32*, 2108–2121. [CrossRef]
15. Zhao, J.; Wu, B. Working mechanism and stability design methods of buckling-restrained braces. *J. Earthq. Eng. Eng. Vib.* **2009**, *29*, 976–992.
16. Wu, B.; Lu, J.; Mei, Y.; Zhang, J. Buckling mechanism and global stability design method of buckling-restrained braces. *J. Constr. Steel Res.* **2017**, *138*, 473–487. [CrossRef]
17. Zhao, J.; Lin, F.; Wang, Z. Seismic design of buckling-restrained brace welded end connection considering frame action effects: Theoretical, numerical and practical approaches. *Eng. Struct.* **2017**, *132*, 761–777. [CrossRef]
18. Wantanabe, A.; Hitomoi, Y. Properties of brace encased in buckling-restraining concrete and steel tube. In Proceedings of the Ninth World Conference on Earthquake Engineering, Tokyo, Japan, 2–9 August 1988.
19. Dongbin, Z.; Xin, N.; Peng, P.; Mengzi, W.; Kailai, D.; Yabin, C. Experimental study and finite element analysis of a buckling-restrained brace consisting of three steel tubes with slotted holes in the middle tube. *J. Constr. Steel Res.* **2016**, *124*, 1–11. [CrossRef]
20. Dusicka, P.; Tinker, J. Global restraint in ultra-lightweight buckling-restrained braces. *J. Compos. Constr.* **2013**, *17*, 139–150. [CrossRef]
21. Taranath, B. Seismic Provisions for Structural Steel Buildings, ANSI/AISC 341-10. In *Structural Analysis and Design of Tall Buildings*; CRC Press: Boca Raton, FL, USA, 2016.
22. Xu, Z.; Yuan, G.; Liu, M.; Shu, Q.; Zhao, Z.; Wang, Z. Effect of vertical location of post-opening on seismic behaviour of RC shear wall: Experimental and numerical analysis. *Case Stud. Constr. Mater.* **2024**, *21*, e03940. [CrossRef]
23. Xia, Y.; Li, X.; Xie, T.; Zhu, R.; Wang, G.; Yi, G.; Li, J. Seismic performance of RC bent columns: Experimental, numerical and life-cycle cost analysis. *Case Stud. Constr. Mater.* **2024**, *20*, e02692. [CrossRef]
24. Yang, J.; Li, L.-Z.; Wang, X.; Hu, S.-X. Experimental study on the seismic performance of concrete shear walls partially replaced by MRPC. *Case Stud. Constr. Mater.* **2024**, *20*, e02695. [CrossRef]
25. Rahnavard, R.; Naghavi, M.; Aboudi, M.; Suleiman, M. Investigating modeling approaches of buckling-restrained braces under cyclic loads. *Case Stud. Constr. Mater.* **2018**, *8*, 476–488. [CrossRef]
26. Luo, Z.; Yu, N.; Li, Z.; Wang, Y. Experimental and numerical investigations on the mechanical properties of precast segmental barriers with UHPC connections. *Case Stud. Constr. Mater.* **2024**, *20*, e03313. [CrossRef]
27. Wei, Y.; Wang, X.; Zhai, C.; He, Y.; Jin, W. Numerical analysis of innovative layered infilled RC frames with rice husk-magnesium oxysulfate cement (RMOC) masonry. *J. Build. Eng.* **2025**, *102*, 111952. [CrossRef]
28. Pan, P.; Deng, K.; Xu, X.; Ye, L.; Xie, J. Experimental study on the mechanical properties of GFRP-steel buckling-restrained braces. *China Civ. Eng. J.* **2014**, *47*, 1–8.

Disclaimer/Publisher's Note: The statements, opinions and data contained in all publications are solely those of the individual author(s) and contributor(s) and not of MDPI and/or the editor(s). MDPI and/or the editor(s) disclaim responsibility for any injury to people or property resulting from any ideas, methods, instructions or products referred to in the content.